International Journal of Nanomedicine

Dovepress
open access to scientific and medical research

Open Access Full Text Article

ORIGINAL RESEARCH

Low Intensity Focused Ultrasound Ignited "Deep-Penetration Nanobomb" (DPNB) for Tetramodal Imaging Guided Hypoxia-Tolerant Sonodynamic Therapy Against Hypoxic Tumors

Yuanli Luo[1,*], Bin Qiao[1,*], Chao Yang[2,*], Ping Zhang[1], Zhuoyan Xie[1], Jin Cao[1], Anyu Yang[1], Qinyanqiu Xiang[1], Haitao Ran[1], Zhigang Wang[1], Lan Hao[1], Yang Cao[1], Zhiyi Zhou[3], Jianli Ren[1]

[1]Chongqing Key Laboratory of Ultrasound Molecular Imaging, the Second Affiliated Hospital of Chongqing Medical University, Chongqing, 400010, People's Republic of China; [2]Radiology Department, Chongqing General Hospital, Chongqing, 400014, People's Republic of China; [3]General Practice Department, Chongqing General Hospital, Chongqing, 400014, People's Republic of China

* These authors contributed equally to this work

Correspondence: Zhiyi Zhou; Jianli Ren, Email renjianli@cqmu.edu.cn; zzy16966@163.com

Background: Sonodynamic therapy (SDT) has been regarded as a novel therapeutic modality for killing tumors. However, the hypoxic tumor microenvironment, especially deep-seated tumors distant from blood vessels, severely restricts therapeutic efficacy due to the oxygen-dependent manner of SDT.

Methods: Herein, we report a novel ultrasonic cavitation effect-based therapeutic modality that is able to facilitate the hypoxia-tolerant SDT for inducing hypoxic tumor death. A tLyP-1 functionalized liposomes is fabricated, composed of hematoporphyrin monomethyl ether gadolinium as the sonosentizer and perfluoropentane (PFP) as the acoustic environment regulator. Moreover, the tLyP-1 functioned liposomes could achieve active tumor homing and effective deep-penetrating into hypoxic tumors. Upon low intensity focused ultrasound (LIFU) irradiation, the acoustic droplet vaporization effect of PFP induced fast liquid-to-gas transition and quick bubbles explosion to generate hydroxyl radicals, efficiently promoting cell death in both normoxic and hypoxic microenvironment (acting as deep-penetration nanobomb, DPNB).

Results: The loading of PFP is proved to significantly enhance the therapeutic efficacy of hypoxic tumors. In particular, these DPNB can also act as ultrasound, photoacoustic, magnetic resonance, and near-infrared fluorescence tetramodal imaging agents for guiding the therapeutic process.

Conclusion: This study is the first report involving that liquid-to-gas transition based SDT has the potential to combat hypoxic tumors.

Keywords: tetramodal imaging, low intensity focused ultrasound, sonodynamic therapy, deep-penetration, hypoxic tumors

Introduction

Photodynamic therapy (PDT) has shown great promise in combating tumors, which employs light to activate the photosensitizers and produce highly toxic reactive oxygen species (ROS).[1–3] It features the advantages of non-ionization, easy controllability, high efficiency, and low cost. However, the efficacy of PDT seriously depends on the penetration depth of light.[4,5] As a mechanical wave, ultrasound (US) has been widely used in the biomedical field, including diagnostic imaging (US imaging) and therapeutic applications (sonodynamic therapy, SDT). Sonosensitizers in SDT generate ROS that promote cell apoptosis and necrosis by low-energy ultrasound activation rather than light energy activation. SDT retains traditional PDT advantages and has a specific killing effect on deep-seated tumors due to the high-penetration US.[6–8] Although promising, the dense tumor stroma, increased interstitial fluid pressure, and disordered vasculature in tumors, especially

Received: 22 February 2022
Accepted: 31 August 2022
Published: 27 September 2022

deep-seated tumors, could lead to insufficient nanomedicine accumulation, which is not conducive to initiate SDT for tumor therapy.[9–11] Moreover, deep-seated solid tumor cells distant from blood vessels often suffer from insufficient oxygen supply due to tissue oxygen content's attenuation.[12–14] Considering the highly oxygen-dependent manner of SDT, the therapeutic outcome is severely restricted in deep-seated tumors. Therefore, it is necessary, urgent, but challenging to develop a deep-penetration system, which can efficiently induce hypoxic tumor cell death.

Many efforts have been proposed to overcome tumor hypoxia, including delivering oxygen into tumors,[15–17] in-situ oxygen generation,[18–20] reducing oxygen consumption,[21–23] and hypoxia-activated prodrugs chemotherapy.[24–26] However, most strategies show limited efficacy in hypoxic tumors and encounter tremendous challenges for clinic applications. Recently, an oxygen-independent free radicals generation strategy is proposed, which employs thermal decomposable initiators (e.g. 2,2-azobis[2-(2-imidazoline-2-yl) propane)] dihydrochloride, benzoyl peroxide, azodiisobutyronitrile, etc.) to generate free radicals for eradiating hypoxic tumors.[8,27,28] Although promising, low initiator's loading capability and high decomposition temperature unavoidably lead to insufficient free radicals generation and diffusion for treating hypoxic tumors. Fortunately, the emergence of ultrasound (US) nanomedicine might provide an ideal choice for constructing next-generation nanoagents to achieve efficient hypoxic tumor therapy, which has been rarely reported.

In contrast to traditional US microbubbles, perfluoropentane (PFP), as a "liquid-to-gas" phase transitional material, was encapsulated in liposomes to prolong their half-life in vivo for effective accumulation in the tumor site.[29–31] Acoustic droplet vaporization (ADV) effect could induce a fast phase-transition manner, converting liquid phase PFP into gas phase under ultrasound triggering. We can observe a significantly augmented US and contrast-enhanced ultrasound imaging (CEUS) signal intensity.[32,33] Generally, the collapse of bubbles under the treatment of US beams could induce an inert cavitation effect and enhance the therapeutic impact via inherent physical factors, including sheer streets, shock waves, microjets, and ROS production multilevel mechanisms due to their intrinsic mechanical-wave nature. Considering microbubbles could increase the efficacy of high-intensity focused ultrasound (HIFU) ablation with reduced acoustic energy and enhanced pathological lesion in tumor treatment, the phase transitional material with similar therapeutic behavior is anticipated to regulate the acoustic environment in hypoxic tumors.[34,35] Notably, the acoustic environment's change has been continuously developed as advanced oxidation processes for wastewater remediation by oxidizing hazardous organic compounds, which is featured by more efficient cavitation effect and ROS production in anoxic condition with the assistance of N_2 than that in the oxic state.[36–38] This industrial technology inspires us to develop a theranostic system to combat hypoxic tumors; along this line, we anticipate that PFP based cavitation effect could serve as a newborn strategy for efficiently inducing hypoxic tumor death without the need to deliver oxygen. Moreover, all these approaches still cannot effectively solve deep-seated tumors due to insufficient nanomedicine accumulation. CGNKRTR (tLyP-1), a kind of cell-penetrating peptide, has been regarded as a ligand targeted to the neuropilin-1 receptor (NPR-1) with high affinity and specificity and can penetrate deep-seated tumor cells effectively through endocytic/exocytic transport pathway (CendR pathway).[11,31,39] As a result, it is a tendency to integrate deep-penetration peptide into a nanomedicine and explore a fresh therapeutic method toward deep-seated hypoxic tumors by regulating acoustic tumor microenvironment.[40–42]

In recent years, photosensitizers have shown great promise in tumor theranostics due to their advantages in photoacoustic (PA) imaging and near-infrared fluorescence (NIRF) imaging.[43–46] NIRF holds the benefits of monitoring the distribution of NPs in the whole body with high sensitivity and short acquisition time. Comparatively, PA can provide images with higher contrast and spatial resolution due to the optical absorption. Although promising, the integration of PA and NIRF still lacks deep-tissue penetration and detailed anatomic information. Both US and magnetic resonance (MR) imaging could achieve deep-seated tumor imaging with high resolution nonradiatively. Simultaneously, the US could rapidly diagnose diseases at a low cost, and MR could provide high spatial information without penetration limited. Therefore, the integration of all these imaging modalities into a single nanoplatform is highly expected to obtain complementary information and achieve "mistake-free diagnosis" in a tailor-made "all-in-one" contrast agent.[47,48]

Herein, we report, for the first time, a LIFU triggered hypoxic-tolerant sonotherapeutic strategy to combat deep-seated hypoxic and normoxic tumors indiscriminately under multimodal imaging guidance. tLyP-1 functionalized phase-transition liposomes was successfully prepared in this strategy, which can actively target MDA-MB-231 tumor

cells and subsequently penetrate deeply into the tumors. Moreover, hematoporphyrin monomethyl ether gadolinium (H(Gd)), as the sonosensitizer, was loaded in phospholipid bilayer (designated as PFP@tLyP-1-LIP-H(Gd)) to initiate the SDT process. Notably, PFP, acting as the main functional phase transitional materials to achieve efficient "liquid-to-gas" transformation under an ADV mechanism, can serve as ideal materials to exert a "bomb-like" therapeutic effect on tumor cells under LIFU irradiation without oxygen-dependence. Because of the excellent targeting abilities and deep penetrating capabilities, tLyP-1 functionalized phase transitional nanoparticles performed the functions of a "deep-penetration nanobomb" for combating tumors. When irradiated with LIFU, which is targeted and focused, PFP@tLyP-1-LIP-H(Gd) could transform from liquid to gas and subsequently achieve contrast-enhanced ultrasound imaging and induce cell death via cavitation effect and SDT effect. Therefore, the LIFU activated PFP@tLyP-1-LIP-H(Gd) could realize hypoxic-tolerant sonodynamic therapy, which provided a low-cost and efficient approach against hypoxic tumors. Unlike other versatile nanoagents that integrate theranostic iron via either encapsulated in the shell or modified on the surface of NPs, Gd^{3+} was previously incorporated into the matallohematoporphyrin monomethyl ether. H(Gd) was used as sonosensitizers because of its high potent in PA/MRI dual-modal imaging and NIRF imaging was achieved after doping hydrophobic fluoroprobe DiR without additional modifications. Therefore, PFP@tLyP-1-LIP-H(Gd), which acts as a "Deep-Penetration Nanobomb" (DPNB), will enable a US/NIRF/PA/MRI tetramodal imaging-guided hypoxic-tolerant sonodynamic therapy against hypoxic tumors (Figure 1).

Materials and Methods

Materials

Dipalmitoyl phosphatidylcholine (DPPC), dipalmitoyl phosphatidylglycerol (DPPG), distearoyl phosphatidyl ethanolamine-polyethylene glycol–maleimide (DSPE-PEG3400-mal), and ethanolamine-polyethylene glycol (DSPE-PEG3400) were purchased from Avanti Polar Lipids Inc. tLyP-1 was obtained from Chinapeptide. Perfluoropentane (PFP) was purchased from Elf Atochem. Dulbecco's modified eagle medium (DMEM) cell culture medium and fetal bovine serum (FBS) were purchased from Sigma-Aldrich Co. (USA). 2-(4-Amidinophenyl)-6-indolecarbamidinedihydrochloride (DAPI) was bought from Beyotime Technology. Agarose was purchased from Invitrogen (Thermo Fisher Scientific). Calcein AM and propidium iodide (PI) and cell counting kit-8 (CCK-8) assay were obtained from Dojindo (Japan). All the chemical reagents in this study were analytical grade and used without any purification.

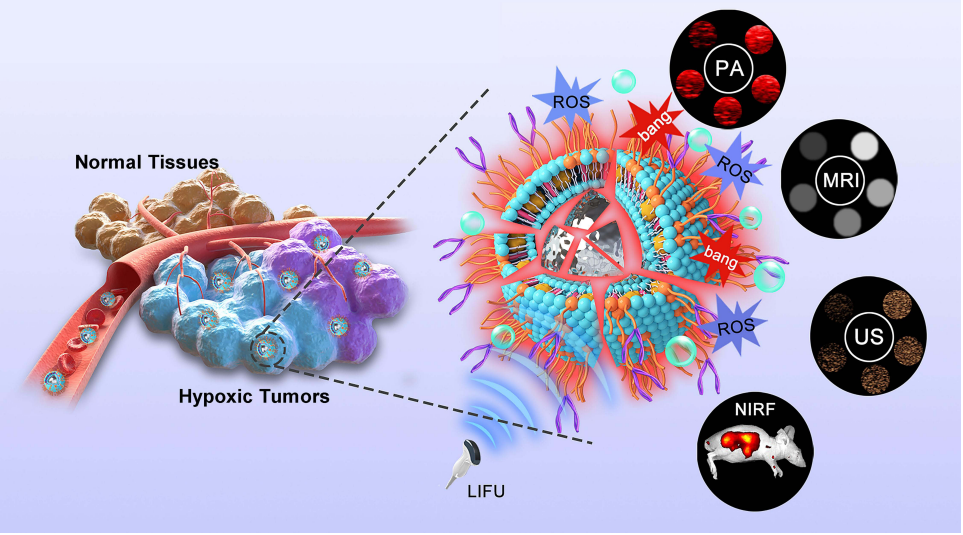

Figure 1 The generation of ROS and ADV mechanisms for synergistic hypoxia-tolerant sonodynamic therapy against solid hypoxic tumors under multimodal imaging guidance. The PFP@tLyP-1-LIP-H(Gd) could actively target the tumor site and penetrate deeply into the tumors, which exerts a "bomb-like" ADV effect and SDT mechanisms to destroy tumor cells under the irradiation of low intensity focused ultrasound (LIFU).

Preparation of PFP@tLyP-1-LIP-H(Gd), PFP@LIP-H(Gd) and PFP@LIP

PFP@tLyP-1-LIP-H(Gd), PFP@LIP-H(Gd), and PFP@LIP were prepared by a facile one-step filming-rehydration method. To prepare PFP@tLyP-1-LIP-H(Gd), DSPE-PEG3400-tLyP-1 was firstly synthesized by Chongqing Protein Way Biotechnology Co. LTD. via a maleimide-thiol coupling reaction. Briefly, 10 mg DPPC, 4 mg DSPE-PEG3400-tLyP-1, 3 mg DPPG, 3 mg cholesterol were dissolved in 10 mL trichloromethane and 2 mg H(Gd) was dissolved in 10 mL methyl alcohol, and the mixture was transferred into a round-bottomed flask. After rotary vacuum evaporation at 50°C for 1 h, a uniform layer film was fabricated. After that, 4 mL PBS was used to rehydrate the film, and 400 μL PFP was added under pulsed sonication (100 W, 5 s on, and 5 s off) for 6 min in an ice bath. Finally, the PFP@tLyP-1LIP-H(Gd) was fabricated after repeated centrifugation (8000 rpm, 10 min) and stored at 4 °C for further use. To prepare PFP@LIP-H(Gd), DSPE-PEG3400 was used to replace DSPE-PEG3400-tLyP-1 with the same additive dose. PFP@LIP was ready with the same method except for the addition of H(Gd).

Loading Efficiency Calculation of H(Gd)

UV-Vis spectra measured the H(Gd) content and organic aqueous phases in the supernatant after repeated centrifugation. The standard curve of H(Gd) was established by detecting the absorbance curves at various concentrations. Loading efficiency of H(Gd) was calculated as follows: Loading efficiency (%) = weight of encapsulated H(Gd)/total weight of H(Gd) × 100 %.

In vitro US/PA/MRI/NIRF Tetramodal Imaging

To evaluate the US imaging capability of PFP@tLyP-1-LIP-H(Gd) in vitro, a 3 % agar (w/v) gel mold was carried out as a test model. First, PFP@tLyP-1-LIP-H(Gd) with the concentration of 0.25 mg mL^{-1} dispersed in 1 mL of solutions were placed and set in the gel. Both B-mode and CEUS-mode were performed to evaluate the imaging properties (Vevo LAZR, Canada). After that, the NPs were exposed to the various intensity of LIFU (0, 0.8, 1.6, and 3.2 W cm^{-2}) for different times (1, 2, 3, and 4 min). The images of the samples were collected. The signal intensity of each sample was determined by the software provided by the imaging system.

To evaluate the PA imaging capability of PFP@tLyP-1-LIP-H(Gd) in vitro, a 3% agar (w/v) gel mold was carried out as a test model. Various concentrations (0.15625, 0.3125, 0.625, 1.25, 2.5, and 5 mg mL^{-1}) of PFP@tLyP-1-LIP-H(Gd) dispersed in 200 μL of solutions were placed in the gel for PA imaging using the same system at the excitation wavelength of 700 nm. The samples' images were collected, and the imaging system's software determined the corresponding signal intensity.

An MR imaging system (Siemens Medical System, Chongqing People's Hospital) at 3.0 T was used to examine the T1-weighted MRI ability in vitro. 2 mL of PFP@tLyP-1-LIP-H(Gd) (with the Gd^{3+} concentration of 0.015– 0.1 mM^{-1}) samples with various concentrations were placed in 4 mL of Eppendorf tubes. The corresponding T1 relaxation time was calculated according to the signal intensity. MR images were obtained using a T1-weighted sequence, and the parameters were set as follows: slice thickness = 3 mm, 320×320 matrices, repetition time (TR)/echo time (TE)=790/15 ms.

A Xenogen IVIS Spectrum Imaging System (PerkinElmer, USA) was employed to evaluate the NIRF imaging ability in vitro. 200 μL of DiR labeled PFP@tLyP-1-LIP-H(Gd)(0.01– 5 mg mL^{-1}) samples with various concentrations were placed in a 96-well plate, and NIRF images were collected at the excitation wavelength of 790 using an 845 nm filter.

Cell Culture and Tumor Xenograft Models

MDA-MB-231 cells and HUVEC cells were obtained from Chongqing Key Laboratory of Ultrasound Molecular Imaging, which were approved by committee of Chongqing Medical University. Cells were cultured in a DMEM medium supplemented with 10 % fetal bovine serum and 1 % penicillin-streptomycin. Healthy female balb/c nude mice (6 weeks old) were purchased from Beijing Huafukang Biotechnology. This study's protocols were conducted following the protocol approved by the department of animal care and use committee of Chongqing Medical University according to the guidelines (GB_T 35892–2018). The tumor xenograft models were established by subcutaneous injection of MDA-MB-231 cells (2×10^6 dispersed in 100 μL of PBS solution) into each mice's right hind limb.

In vitro Active-Targeting Effect of PFP@tLyP-1-LIP-H(Gd)

MDA-MB-231 cells and HUVEC cells were seeded in CLSM-specific cell culture dishes (1×10^5 cells per well) and cultured for 24 h to adhere to the dish's wall to investigate the active targeting effect of PFP@tLyP-1-LIP-H(Gd). Then PFP@tLyP-1-LIP-H(Gd) or PFP@LIP-H(Gd) dispersed in DMEM (1 mg mL^{-1}) was added into each well and incubated various times (0.5, 1, 2, and 4 h). After that, the cells were washed with fresh DMEM three times and incubated with DAPI for another 15 min. Finally, the cells were fixed with 4% paraformaldehyde and observed under CLSM (Nikon A1, Japan). To build the three-dimensional spheroids, MDA-MB-231 cells (10^5 mL^{-1}) were seeded into agarose-coated plates. 10 days later, the spheroids were created for further use. After that, 250 μg mL^{-1} of DiI-labeled nanoparticles were introduced to the plates containing spheroids. After 24 hours of incubation, spheroids were rinsed three times with PBS and fixed for 30 minutes with 4 % paraformaldehyde. CLSM was used to observe the fluorescence intensity at different depths of spheroids.

To further evaluate the uptake behavior of MDA-MB-231 cells and HUVEC cells, the cells were seeded (1×10^5 cells per well). After 24 h incubation, PFP@tLyP-1-LIP-H(Gd) or PFP@LIP-H(Gd) were added and incubated for different times (0.5, 1, 2, and 4 h) respectively. Then the medium was discarded, and the cells were washed with fresh DMEM. The intracellular uptake behavior was analyzed with flow cytometry.

In vitro ROS Production Under the Irradiation of LIFU

3 mL of PFP@tLyP-1-LIP at a concentration of 1 mg mL^{-1} containing methylene blue (10 μg mL^{-1}) was added into an eppendorf tube and irradiated with LIFU (1.6 W cm^{-2}) for different time intervals (5, 10, 15, 20, and 25 min) followed by observation with a UV-Vis spectrometer ranging from 500–750 nm. Moreover, 3 mL of different NPs at various concentrations containing SOSG (50×10^{-6} M) was added into a cuvette and irradiated with LIFU (1.6 W cm^{-2}) for a different time interval followed by observation with a multimode reader. MDA-MB-231 cells were incubated with different NPs (2 mg mL^{-1}) for 4 h. Then the cells were incubated with fresh DMEM medium (containing 10 μM of DCFH-DA) at 37°C for 20 min. Then the cells were exposed to LIFU (1.6 W cm^{-2}, 2 min) and observed by CLSM. The cells were put in a GENbox Jar to a hypoxic group until the color of the anaerobic indicator changed from pink to colorless.

In vitro Synergistic Therapeutic Effect Induced by LIFU

MDA-MB-231 cells were seeded in 96-well plates (1×10^4 per well) and cultured overnight to evaluate the therapeutic effect of NPs in both normoxic and hypoxic conditions. Then the medium was replaced by fresh DMEM with various concentrations with PFP@tLyP-1-LIP-H(Gd), PFP@tLyP-1-LIP, and tLyP-1-LIP, respectively. The NPs concentrations were ranged from 0.375–3.0 mg mL^{-1}. After 4 h incubation, the cells were treated with LIFU (1.6 W cm^{-2}, 3 min) and cultured for another 8 h. Cells without irradiation with LIFU were set as controls. For the hypoxic group, the cells were treated with identical conditions except for the GENbox Jar treatment. The environment would become hypoxia since the indicator's color changed from pink to colorless. After that, the samples were washed with fresh DMEM three times and incubated with 10 μL CCK-8 solution for 2 h. The cell viability was determined according to the results obtained from the microplate reader at 450 nm.

MDA-MB-231 cells (1×10^4 per well) were seeded in CLSM-specific plates and cultured for 12 h to adhere to the plate. PFP@tLyP-1-LIP-H(Gd), tLyP-1-LIP-H(Gd), and PFP@LIP-H(Gd) were added respectively and coincubated for 4 h and exposed to LIFU (1.6 W cm^{-2}, 3 min). After another 6 h, the cells were stained with Calcein-AM and PI for 15 min and imaged by CLSM.

In vivo NIRF/US/PA/MRI Tetramodal Imaging

The MDA-MB-231 tumor-bearing mice were intravenously injected with DiR labeled-PFP@tLyP-1-LIP-H(Gd) or PFP@LIP-H(Gd). The images were collected at different times (0, 2, 6, 12, and 24 h) postinjection. Moreover, major organs (including heart, liver, spleen, lungs, kidneys, and brain) were collected at 24 h postinjection. The images were observed using a Xenogen IVIS Spectrum Imaging System. The biodistribution of NPs was quantified by the software provided by the Xenogen IVIS Spectrum Imaging System.

For US and PA imaging, the tumor-bearing mice were intravenously injected with PFP@tLyP-1-LIP-H(Gd) or PFP@LIP-H(Gd). The images were collected at different times (0, 2, 6, 12, and 24 h) postinjection. The images were observed using a PA imaging system (Vevo LAZR, Canada). The tumor-site accumulation of NPs was quantified by the software provided by the PA Imaging System. At 2 h postinjection, LIFU was performed to the tumor-site and imaged using the B-mode and CEUS-mode in the PA Imaging System.

For T1-weighted imaging, the tumor-bearing mice were intravenously injected with PFP@tLyP-1-LIP-H(Gd). The mice injected with identical concentrations of PFP@tLyP-1-LIP were set as a control. The images were observed using a 3.0 T MRI imaging system (Siemens Medical System, Chongqing People's Hospital) at different times (4, 6, 12, and 24 h) postinjection. The tumor-site accumulation of NPs was quantified by the software provided by the exact MR Imaging System.

In vivo Synergistic Tumor Therapy and Biocompatibility Evaluation

When the tumors grew to about 80 mm^3 in volume, the tumor-bearing mice were randomly divided into 6 groups (n=6 in each group). The groups were set as follows: 1) Control group, 2) LIFU only group, 3) tLyP-1-LIP+LIFU group, 4) tLyP-1-LIP-H(Gd) + LIFU group, 5) PFP@tLyP-1-LIP-H(Gd) group, 6) PFP@tLyP-1-LIP-H(Gd) + LIFU group. The power intensity of LIFU was set as 1.6 W cm^{-2}, 3 min. The tumor size and body weight were recorded every other day. The representative mice were sacrificed at 1 d post-treatment. The H&E, PCNA and TUNEL staining of tumors were performed to evaluate the therapeutic effect. The biocompatibility was evaluated by H&E staining of the major organs (heart, liver, spleen, lungs, kidneys, and brain). To further assess the in vivo tumor-site accumulation of PFP@tLyP-1-LIP-H(Gd) and PFP@LIP-H(Gd), the tumor-bearing mice were intravenously injected with DiI labeled-PFP@tLyP-1-LIP-H(Gd) or PFP@LIP-H(Gd). The mice were sacrificed at different times (1, 2, 6, 12, and 24 h) postinjection. The tumor-site accumulation of NPs was imaged using CLSM.

Results and Discussion

Preparation and Characterization of PFP@tLyP-1-LIP-H(Gd) NPs (DPNB)

The synthesis scheme of PFP@tLyP-1-LIP-H(Gd) NPs as "DPNB" was shown in (Figure 2A). Our study prepared PFP@tLyP-1-LIP-H(Gd) NPs in a simple one-step emulsion method with a typical core-shell structure with lipid(LIP)/H(Gd) shell and PFP as the core; tLyP-1 was modified on the surface via a maleimide-thiol coupling reaction as the targeting component for active targeting and deep penetration. After sonication in an ice bath and subsequent centrifugation to remove the excess gradients, transmission electron microscopy (TEM) images were obtained. A uniformly distributed core-shell structure of PFP@tLyP-1-LIP-H(Gd) NPs was observed (Figure 2B). The absorbance spectra of H(Gd) with different concentrations were obtained. According to the UV-Vis absorbance values at the wavelength of 411 nm (Figure 2C and D), H(Gd) 's loading efficiency was determined to be 93.3 ± 3.1 % by comparing unloaded H(Gd) to the pre-established standard curve (Figure S1). Moreover, the UV-Vis spectra demonstrated that both PFP@tLyP-1-LIP-H(Gd) and PFP@LIP-H(Gd) retain the absorption peak of H(Gd) at around 400 nm and several specific wavelengths between 450 and 650 nm (Figure 2E). In comparison, PFP@LIP showed a smooth UV-Vis spectrum between 300 and 700 nm without a prominent absorption peak, further indicating the success loading of H(Gd) (Figure 2E). The average diameter of the PFP@tLyP-1-LIP-H(Gd) was 260.9 ± 4.3 nm (PDI=0.016), and the zeta potential was −15.7 ± 2.2 mV according to the dynamical light scattering (DLS) results (Figure 2F and G and Figure S2), which is following the TEM results. Moreover, the zeta potential changed from −29.2 mV to −15.7 mV after decoration with positive potential tLyP-1. These results suggest the successful construction of PFP@tLyP-1-LIP-H(Gd) and meet the criterion for subsequent applications.

In vitro Cell Uptake Behavior of PFP@tLyP-1-LIP-H(Gd)

It has been demonstrated that the cell-penetrating peptide tLyP-1 was responsible for the specific adhesion nature to specific cells that overexpressed NPR-1. The tLyP-1 functionalized nanoplatform could target specific tumors through the endocytic/exocytic transport pathway (CendR pathway). As a result, PFP@tLyP-1-LIP-H(Gd) 's dynamic targeting effect

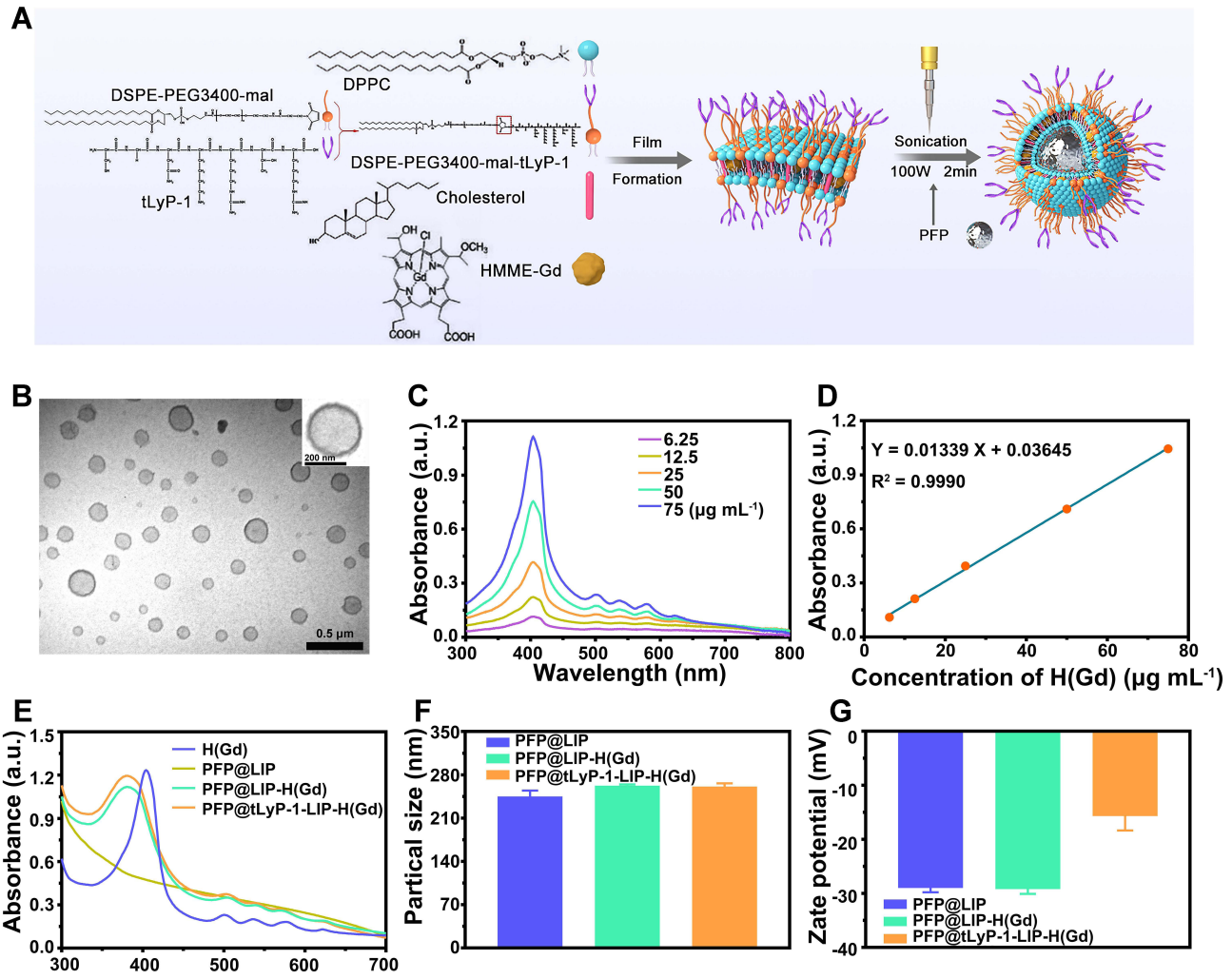

Figure 2 Characterization of PFP@tLyP-1-LIP-H(Gd). (**A**) Schematic illustration of PFP@tLyP-1-LIP-H(Gd) preparation process. (**B**) TEM images of PFP@tLyP-1-LIP-H(Gd). The scale bar is 500 nm, and the insertion scale bar is 200 nm. (**C**) Calibration curve of H(Gd) based on UV-Vis spectra. (**D**) UV-Vis spectra of H(Gd) at different concentrations of H(Gd). (**E**) UV-Vis spectra of H(Gd), PFP@LIP, PFP@LIP-H(Gd) and PFP@tLyP-1-LIP-H(Gd). (**F**) Particle sizes of PFP@LIP, PFP@LIP-H(Gd) and PFP@tLyP-1-LIP-H(Gd). (**G**) Zeta potential of PFP@LIP, PFP@LIP-H(Gd), and PFP@tLyP-1-LIP-H(Gd).

against MDA-MB-231 cells was evaluated using human umbilical vein endothelial cells (HUEVC) as the control. As shown in (Figure 3A), MDA-MB-231 cells showed a much higher fluorescence than that in HUEVC cells in 4 h observation after co-incubation with PFP@tLyP-1-LIP-H(Gd), indicating the specific targeting effect of PFP@tLyP-1-LIP-H(Gd) to MDA-MB-231 cells. Additionally, compared to PFP@LIP-H(Gd) group, PFP@tLyP-1-LIP-H(Gd) group displayed more vigorous fluorescence intensity due to the active targeting effect in the presence of tLyP-1 (Figure 3A). Similarly, it was found that MDA-MB-231 cells exhibited stronger fluorescence in the PFP@tLyP-1-LIP-H(Gd) group than that in PFP@LIP-H(Gd) group; the fluorescence in MDA-MB-231 cells is higher than that in HUEVC cells when treated by PFP@tLyP-1-LIP-H(Gd) with identical treatment as determined by flow cytometry (Figure S3). All these results indicated the active targeting effect of PFP@tLyP-1-LIP-H(Gd) against MDA-MB-231 cells.

In vitro, three-dimensional tumor spheroid is a classical model to mimic the microenvironment of solid tumors. In this study, we established three-dimensional spheroids of MDA-MB-231 cells. After co-incubation with PFP@tLyP-1-LIP-H(Gd) or PFP@LIP-H(Gd) for 24 h, we found that the red fluorescence of PFP@tLyP-1-LIP-H(Gd) distributed more evidently than that of PFP@LIP-H(Gd) in the spheroids. The PFP@tLyP-1-LIP-H(Gd) could reach more than 90 μm away from the bottom of the tumor spheroids, whereas PFP@LIP-H(Gd) only in the surface layer of the tumor spheroids. The above results indicated that tLyP-1 peptide could facilitate the transport of NPs into the deep-seated region of tumors (Figure 3B).

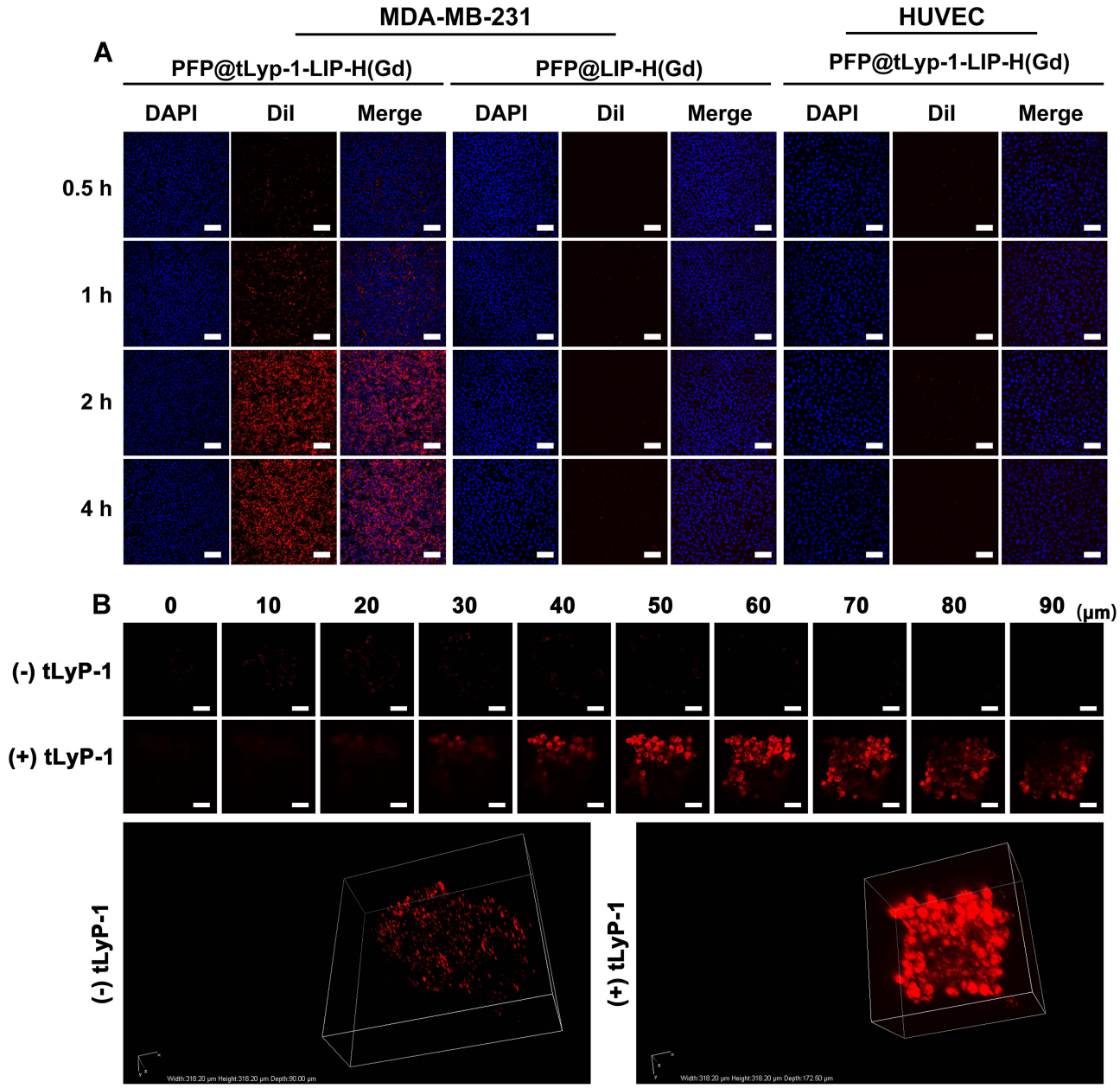

Figure 3 Internalization of PFP@tLyP-1-LIP-H(Gd) in different cell lines. (**A**) Uptake of PFP@tLyP-1-LIP-H(Gd) and PFP@LIP-H(Gd) by MDA-MB-231 cells or HUVEC cells at different incubation times observed by CLSM. (**B**) Three-dimensional reconstruction of the MDA-MB-231 spheroids model incubated with PFP@tLyP-1-LIP-H(Gd) or PFP@LIP-H(Gd). The scale bar is 50μm.

In vitro ROS Generation of PFP@tLyP-1-LIP-H(Gd)

PFP@tLyP-1-LIP-H(Gd) includes a core of the PFP molecule, which could undergo a fast liquid-to-gas transition under LIFU irradiation. Notably, the acoustic environment's change has been continuously developed as advanced oxidation processes for wastewater remediation by oxidizing hazardous organic compounds, which is featured by more efficient cavitation effect and ROS production in anoxic condition with the assistance of N_2 than that in the oxic state.[14] Therefore, we anticipate the gaseous PFP could combat hypoxic tumors by assisting ROS production in anoxic condition. Subsequently, the ROS generation of PFP@tLyP-1-LIP and tLyP-1-LIP in the hypoxia conditions was evaluated by methylene blue, whose fluorescence decreased sharply in the presence of ROS. The ROS generation of PFP@tLyP-1-LIP-H(Gd) was performed in distilled water, which is an environment lack of different kinds of gas and can act as hypoxia conditions. As shown in (Figures 4A and B), PFP@tLyP-1-LIP showed potent ROS generation, in sharp contrast

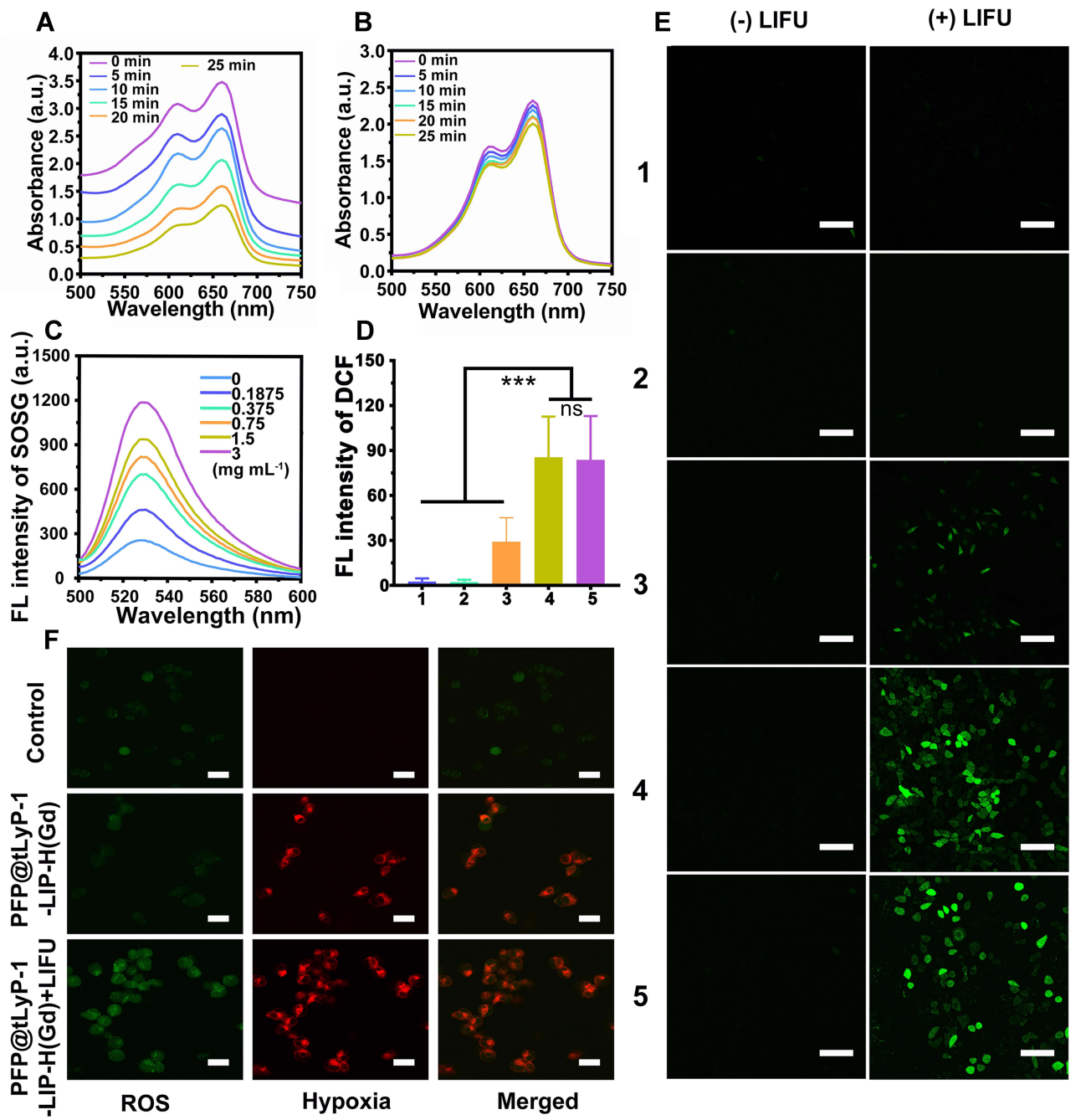

Figure 4 Evaluation of ROS generation. (**A**) PFP@tLyP-1-LIP and (**B**) tLyP-1-LIP. (**C**) Fluorescence spectrum of SOSG under different PFP@tLyP-1-LIP-H(Gd) concentrations at a fixed LIFU intensity (1.0 MHz, 1.6 W cm^{-2}, 120 s). (**D**) Quantitative results of the fluorescence of DCF after different treatment in normoxia and hypoxia and (**E**) corresponding CLSM images. (**F**) ROS production and hypoxia status of MDA-MB-231 cancer cells incubated with PFP@tLyP-1-LIP-H(Gd) with/without LIFU. The scale bar is 50 μm. (group 1: Control, group 2: tLyP-1-LIP(hypoxia), group 3: PFP@tLyP-1-LIP(hypoxia), group 4: PFP@tLyP-1-LIP-H(Gd)(normoxia), group 5: PFP@tLyP-1-LIP-H(Gd)(hypoxia)).(***$p < 0.001$ compared by one-way ANOVA analysis, n=5).

to single tLyP-1-LIP, indicating that PFP can induce ROS generation by cavitation effect in a hypoxia environment. Therefore, we anticipate that PFP based cavitation effect could serve as a newborn strategy for efficiently inducing hypoxic tumor death without the need to deliver oxygen.

The SDT efficiency of PFP@tLyP-1-LIP-H(Gd) was then confirmed with singlet oxygen sensor green (SOSG) as the ROS indicator in vitro, whose fluorescence increased sharply in the presence of ROS. First, the ROS production was determined by testing fluorescence intensity at various concentrations and prolonged LIFU irradiation duration. We found

that the SOSG fluorescence in PFP@tLyP-1-LIP-H(Gd) NPs exhibits a concentration-dependent manner at selected time points after LIFU irradiation (Figure 4C). Interestingly, PFP@tLyP-1-LIP-H(Gd) also showed an irradiation duration-dependent ROS generation manner at a fixed concentration of PFP@tLyP-1-LIP-H(Gd) (Figure S4), which could benefit the precise control of SDT efficiency for personal requirements. The highly efficient ROS production of PFP@tLyP-1-LIP-H(Gd) in solution inspired us to investigate the cellular level's SDT efficiency further under hypoxic conditions. 2'-7'-dichlorodihydrofluorescein diacetate (DCFH-DA) was used as the indicator, whose fluorescence would be turned on and produce fluorescence DCF by ROS, to evaluate SDT efficacy. As shown in (Figure 4D and E), compared to PFP@tLyP-1-LIP, PFP@tLyP-1-LIP-H(Gd) showed a more remarkable ROS production ability with higher DCF fluorescence, which can ascribe to the SDT effect after loading H(Gd). Moreover, PFP@tLyP-1-LIP showed an enhanced ROS production compared to tLyP-1-LIP, confirming ROS generation of PFP@tLyP-1-LIP originated from the cavitation effect during the phase-transition process in the presence of PFP. To estimate the ROS production in a hypoxia environment, we evaluated the SDT efficiency under the same conditions. After LIFU irradiation, a comparable green fluorescence was observed in hypoxia compared to that in normoxia, confirming the ROS generation by PFP@tLyP-1-LIP-H(Gd) is hypoxia-tolerant (Figure 4D and E). In the groups without LIFU irradiation, no noticeable fluorescence could be observed under the same condition. These results revealed that NPs alone without LIFU irradiation could not induce ROS generation, indicating the controlled ROS release ability of PFP@tLyP-1-LIP-H(Gd). These results showed PFP@tLyP-1-LIP-H(Gd) potential as sonosensitizers and cavitation nuclei to achieve hypoxia-tolerant sonodynamic therapy against cancer cells. A hypoxia/oxidative stress detection kit confirmed the hypoxic environment in vitro and intracellular ROS generation (Figure 4F).

LIFU Activated SDT and "Bomb-Like" Cavitation Effect of PFP@tLyP-1-LIP-H(Gd)

Having proved the hypoxia-tolerant ROS generation based on the cavitation effect in the presence of PFP, the therapeutic efficacy of PFP@tLyP-1-LIP-H(Gd) was evaluated by a standard CCK-8 assay. MDA-MB-231 cells were chosen as the representative cell line to assess the cytotoxicity of PFP@tLyP-1-LIP-H(Gd) under normoxia and hypoxia environment. First, the biocompatibility of PFP@tLyP-1-LIP-H(Gd), PFP@LIP-H(Gd), and PFP@LIP NPs were tested, and negligible cytotoxicity was observed (Figure S5), indicating the high biocompatibility of the NPs. Subsequently, the antitumor efficacy of PFP@tLyP-1-LIP-H(Gd), tLyP-1-LIP-H(Gd), and tLyP-1-LIP were assessed after treatment with LIFU under normoxic and hypoxic condition. As expected, PFP@tLyP-1-LIP showed enhanced cytotoxicity compared to tLyP-1-LIP, indicating the cavitation effect of PFP@tLyP-1-LIP post "liquid-to-gas" phase-transitional process could induce cell death more efficiently under our testing conditions (Figure 5A and B). Moreover, the PFP@tLyP-1-LIP + LIFU group's cell viability was significantly lower than that in the PFP@tLyP-1-LIP-H(Gd) + LIFU group at the same concentration, indicating the SDT effect in the presence of H(Gd). Furthermore, the SDT effect of PFP@tLyP-1-LIP-H(Gd) was higher than that of PFP@LIP-H(Gd) due to the active targeting efficacy originated from tLyP-1 as mentioned above (Figure S6). Notably, for the PFP@tLyP-1-LIP groups, both hypoxia and normoxia environments showed comparable therapeutic efficacy in MDA-MB-231 cells, indicating the hypoxia-tolerant therapeutic process induced by the cavitation effect (Figure 5A and B). To examine the therapeutic effect of LIFU more intuitively, CLSM was carried out, and minimal cell death was observed for all groups without LIFU irradiation (Figure 5C). Moreover, the tLyP-1-LIP-H(Gd)+LIFU group showed minimal therapeutic effect under hypoxia. In contrast, PFP@tLyP-1-LIP-H(Gd) showed the most cell death in both hypoxia and normoxia conditions after LIFU irradiation, further proving the hypoxia-tolerant therapeutic efficacy of SDT in inducing cell death against hypoxic tumors, which was following the CCK-8 results.

In vitro US/NIRF/PA/MRI Tetramodal Imaging Capability

PFP is a "liquid-to-gas" phase transitional material and acoustic droplet vaporization effect could induce a fast phase-transition manner, converting liquid phase PFP into gas phase under ultrasound triggering. Herein, the cavitation effect induced by the acoustic droplet vaporization effect was intuitively observed by a microscope (Figure 6A). PFP@tLyP-1-LIP-H(Gd) includes a core of the PFP molecule, which could undergo a fast liquid-to-gas transition under LIFU irradiation. After LIFU irradiation, PFP@tLyP-1-LIP-H(Gd) realized a gradual increase in size compared to the control NPs for a prolonged duration of 1–4 min at the power intensity 1.6 W cm^{-2}. In vitro therapeutic efficacy of PFP@tLyP-

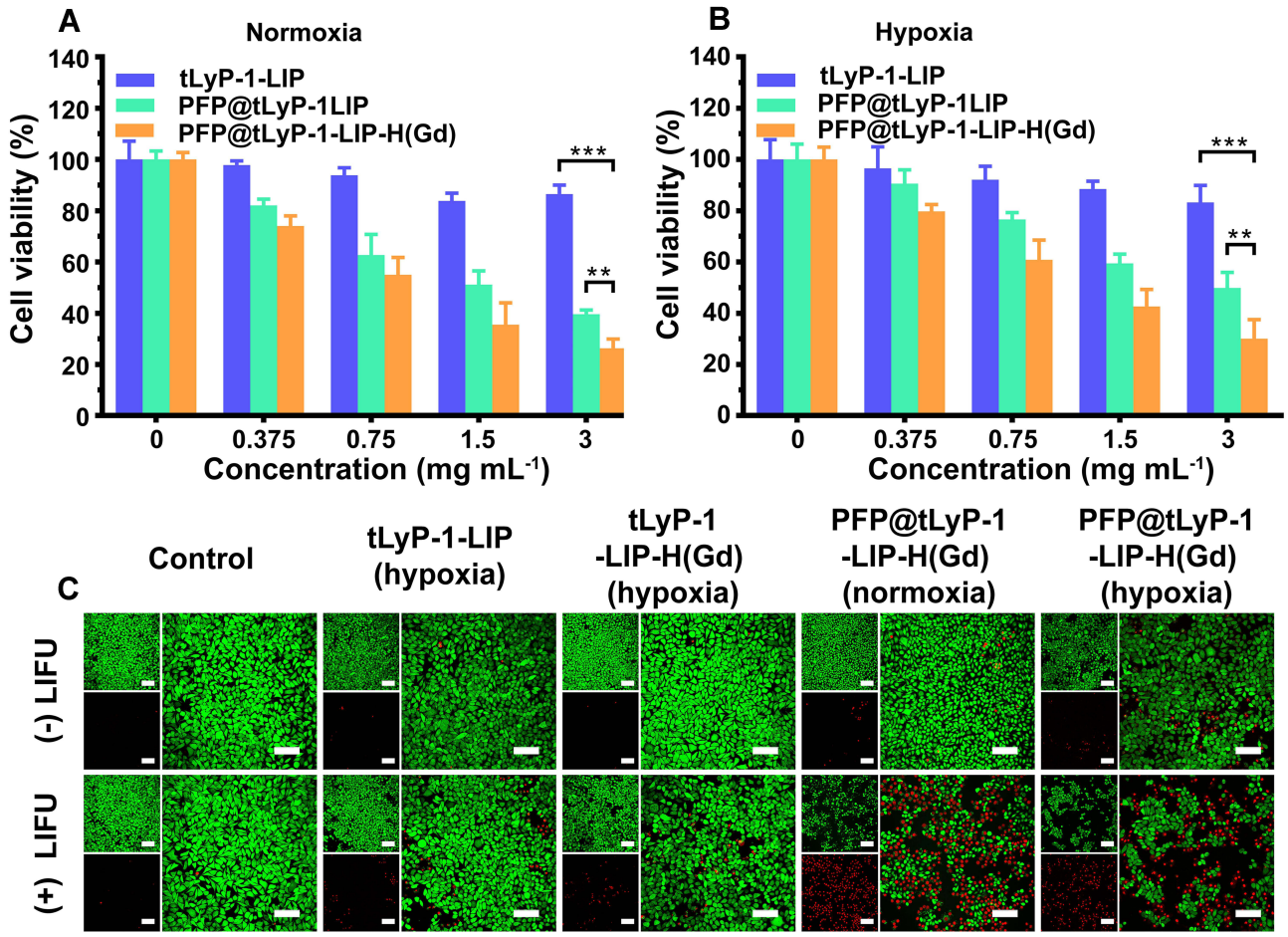

Figure 5 In vitro cell experiments. LIFU induced therapeutic efficacy of PFP@tLyP-1-LIP-H(Gd), PFP@tLyP-1-LIP, and tLyP-1-LIP in MDA-MB-231 cells under (**A**) normoxia and (**B**) hypoxia. (**C**) CLSM images of MDA-MB-231 cells were costained with Calcein AM (green fluorescence) and PI (red fluorescence) after different treatments in normoxia and hypoxia. The scale bar is 50 μm. (**$p < 0.01$, ***$p < 0.001$ compared by one-way ANOVA analysis, n=5).

1-LIP-H(Gd) has demonstrated the inert cavitation effect enhanced sonodynamic therapy at the cellular level in both normoxia and hypoxia. The produced microbubbles contribute to an enhancement in US imaging, which could be examined using both B-mode and contrast-enhanced ultrasound (CEUS)-mode ultrasound imaging. As expected, we observed an intensified signal increase in both B-mode and CEUS-mode with the increasing irradiation duration in 4 min observations (Figure 6B–D), indicating the presence of phase-transition effect and the formation of gaseous PFP. In contrast, the microbubbles could be further exploded at a higher intensity of LIFU, and a decreased imaging signal was observed due to the sputtering of microbubbles. As a control, tLyP-1-LIP-H(Gd) without the encapsulation of PFP showed no noticeable change in ultrasound signal under ultrasound treatment, suggesting PFP could induce a phase-transition behavior. These results supported the powerful ADV effect and the liquid-gas transition of PFP@tLyP-1-LIP-H(Gd) for US imaging under LIFU irradiation.

To further evaluate the NIRF imaging properties of PFP@tLyP-1-LIP-H(Gd), the various concentration of DiR-labeled PFP@tLyP-1-LIP-H(Gd) were placed in a 96-well plate. The fluorescence of PFP@tLyP-1-LIP-H(Gd) increased in the range of 0.01 mg mL^{-1}–0.3125 mg mL^{-1}; however, the fluorescence remains unchanged in the field of 0.3125 mg mL^{-1}– 5 mg mL^{-1} due to the self-quenching effect of DiR, indicating the effectiveness of PFP@tLyP-1-LIP-H(Gd) as a NIRF contrast for imaging applications (Figure 6E). Moreover, considering the PA signal of H(Gd), we evaluated the PA signal of PFP@tLyP-1-LIP-H(Gd), and it increased linearly with the increasing concentration of PFP@tLyP-1-LIP-H(Gd) (Figure 6F and Figure S7). As classical MRI imaging agents, Gd^{3+} has been widely used as a contrast agent for T_1-weighted MRI of tumors in the clinic. Thus, the MRI imaging of PFP@tLyP-1-LIP-H(Gd) was measured quantitatively. As shown in Figure 6G, a linearly brightening effect was

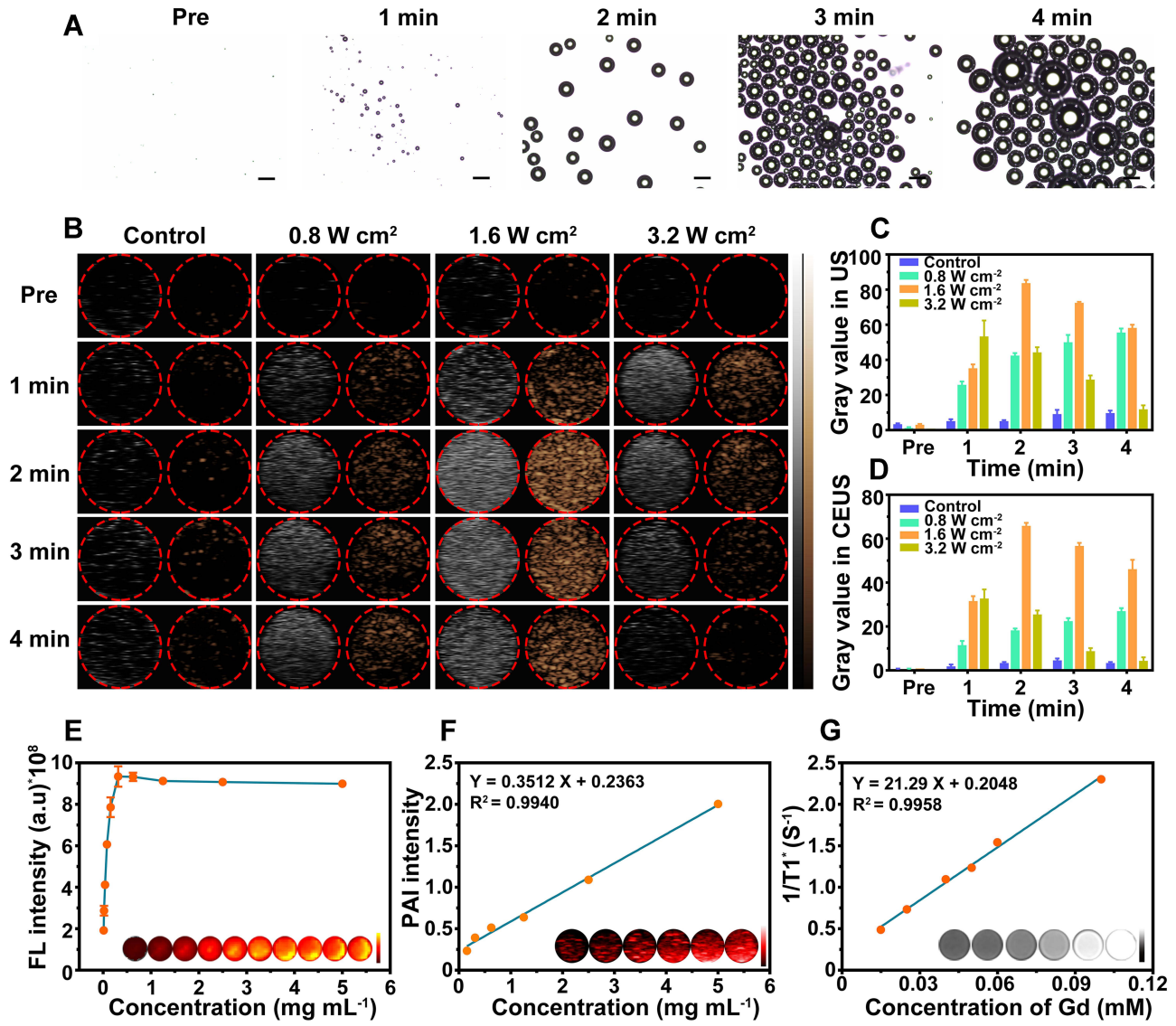

Figure 6 Multimodal imaging capability in vitro. (**A**) Optical microscopy images of LIFU-responsive phase-transition process of PFP@tLyP-1-LIP-H(Gd) at prolonged irradiated durations. (**B**) B-mode and CEUS-mode ultrasound images of PFP@tLyP-1-LIP-H(Gd) under LIFU irradiation with different intensities at different times. Corresponding quantitative echo intensity of (**C**) B-mode and (**D**) CEUS-mode. (**E**) In vitro FL images, (**F**) PA images, and (**G**) MR images at different concentrations.

observed, and the relaxation time was calculated to be 21.29 mM^{-1} s^{-1}. Therefore, the above results demonstrated PFP@tLyP-1-LIP-H(Gd) potential as contrast agents for US/NIRF/PA/MRI tetramodal imaging.

In vivo Active-Targeting Capability and US/NIRF/PA/MRI Tetramodal Imaging

PFP@tLyP-1-LIP-H(Gd)'s targeting effect in vitro inspired us to further examine tumor-specific accumulation in tumor-bearing mice. Fluorescence imaging was first performed to evaluate the bio-distribution in the whole body using DiR-labeled PFP@LIP-H(Gd) as a contrast agent. After intravenous injection of PFP@tLyP-1-LIP-H(Gd) or PFP@LIP-H(Gd), prominent fluorescence was observed in the PFP@tLyP-1-LIP-H(Gd) group at 2 h postinjection and remain steady at the tumor-site in 24 h observation (Figure 7A). However, no obvious fluorescence signal was found in the PFP@LIP-H(Gd) group, which could be ascribed to the enhanced tumor-specific targeting of PFP@tLyP-1-LIP-H(Gd) endowed by tLyP-1. Moreover, the fluorescence signal of tumor ex vivo was also improved in PFP@tLyP-1-LIP-H(Gd) group. Simultaneously, a decreased liver accumulation was observed (Figure 7B and C), which further supported the feasibility of decorating tLyP-1 for tumor-specific accumulation.

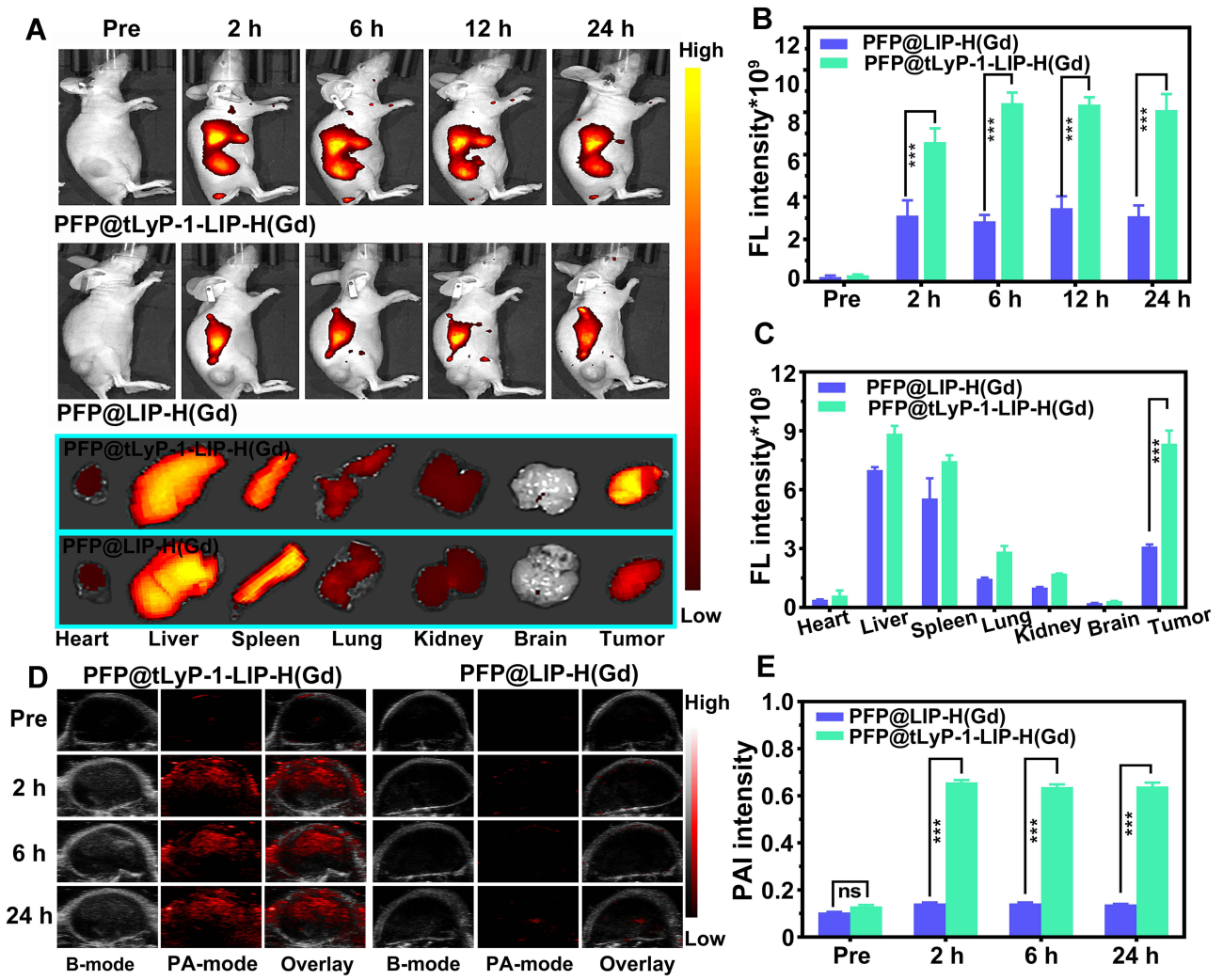

Figure 7 FL and PA imaging capability in vivo. (**A**) In vivo and ex vivo FL images of MDA-MB-231 tumor-bearing mice and ex vivo FL images of major organs (including heart, liver, spleen, lungs, kidneys, and brain). Corresponding quantitative FL intensities are postinjection of different NPs (**B**) in vivo and (**C**) ex vivo. (**D**) PA images of MDA-MB -231 tumor-bearing mice and (**E**) corresponding quantitative PA intensities postinjection of different NPs. (*ns means* $p>0.05$, ***$p < 0.001$ compared by one-way ANOVA analysis, n=3).

The integration of multimodal imaging to achieve a clinical diagnosis, therapeutic guidance, and outcome monitoring is highly desired in tumor theranostics. Considering the US/PA/MRI capability of PFP@tLyP-1-LIP-H(Gd) in vitro, we examined the multimodal imaging capability in vivo. First, PFP@tLyP-1-LIP-H(Gd) was intravenously injected into tumor-bearing mice. The PA intensity in the tumor site is higher postinjection than preinjection (Figure 7D and E). At 2 h postinjection, the PA signal within the tumor increased significantly and remain steady during 24 h observation. Moreover, there was no noticeable change in the PA signal in tumor-bearing treated by intravenous injection of PFP@LIP-H(Gd), indicating the PFP@tLyP-1-LIP-H(Gd)) could accumulate selectively at the tumor site effectively and achieve PA imaging. Second, the MRI imaging capability was then evaluated in tumor-bearing mice. Like PA imaging, the MRI signal intensity in the tumor site showed a noticeable brightening effect 24 h after intravenous injection of PFP@tLyP-1-LIP-H(Gd) (Figure 8A). The quantitative analysis of tumor-site signal intensity showed positive signal enhancement (Figure 8B). As a contrast, minor enhancement in MR imaging was observed after injection of PFP@LIP-H(Gd); therefore, the as-prepared PFP@tLyP-1-LIP-H(Gd) could act as an ideal MRI contrast agent for T1-weighted MRI in vivo.

As for ultrasound imaging, both the B-mode ultrasound and CEUS-mode were evaluated. The results showed a slight enhancement in images at 2 h postinjection of PFP@tLyP-1-LIP-H(Gd), indicating a slight phase-transition of NPs happened

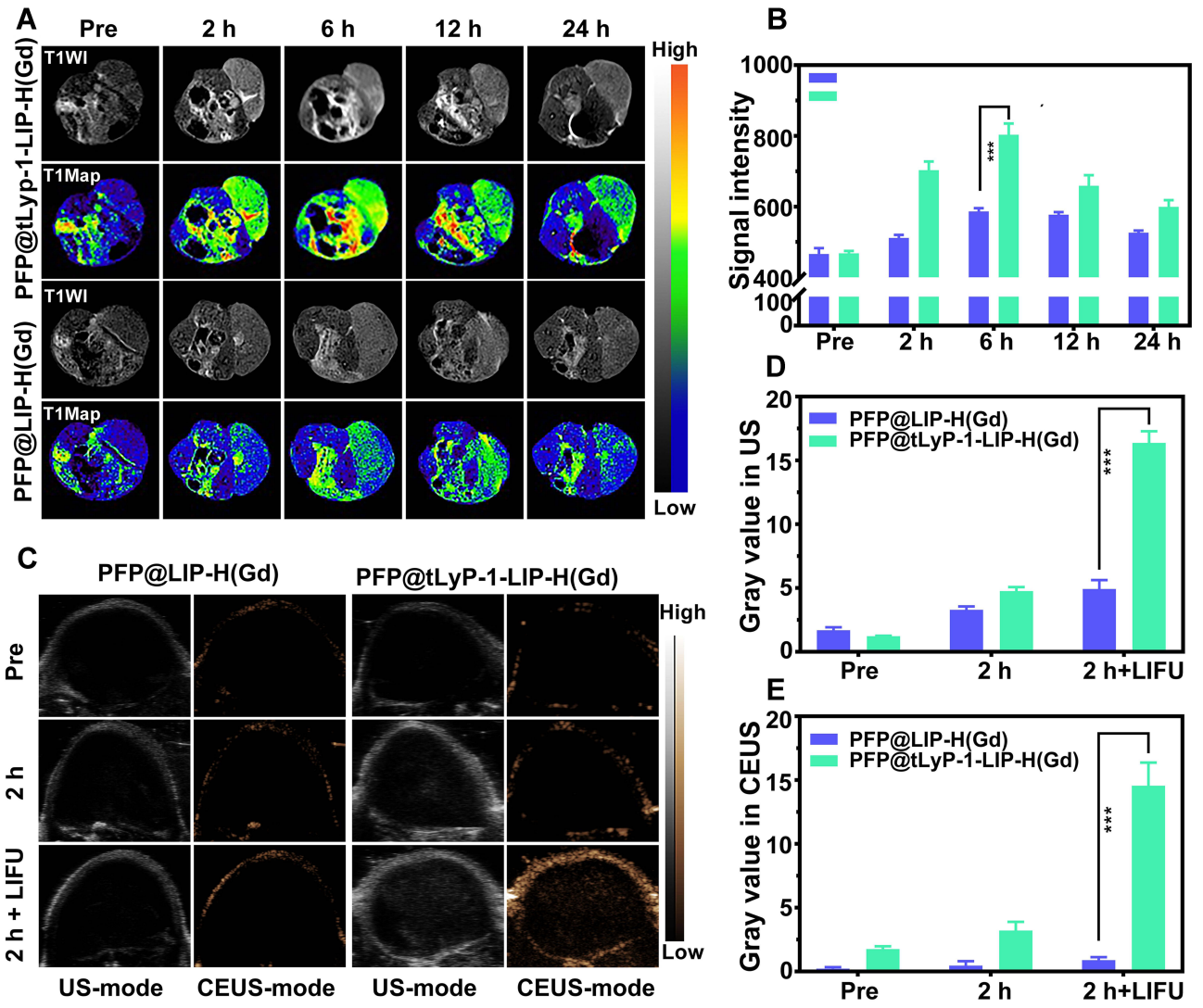

Figure 8 MRI and US imaging capability in vivo. (**A**) MR images of MDA-MB-231 tumor-bearing mice and (**B**) corresponding quantitative MR intensities postinjection of different NPs. (**C**) B-mode and CEUS-mode ultrasound imaging at tumor-site before and after intravenously injecting PFP@LIP-H(Gd) or PFP@tLyP-1-LIP-H(Gd). After 2 h postinjection, the tumors were exposed to LIFU, and US images were obtained in both B-mode and CEUS-mode. Corresponding quantitative US signal intensities in both (**D**) B-mode and (**E**) CEUS-mode. (***$p < 0.001$ compared by one-way ANOVA analysis, n=3).

(Figure 8C). However, the echo signal showed a noticeable enhancement after LIFU irradiation (Figure 8D and E), suggesting that PFP@tLyP-1-LIP-H(Gd) could accumulate into the tumor region effectively and trigger phase-change via ADV effect as discussed above. Therefore, PFP@tLyP-1-LIP-H(Gd) could realize ultrasound imaging and show better enhancement as ultrasound contrast agents, while the decoration of tLyP-1 might be extensive both the imaging and therapeutic effect for advanced applications. Based on the above results, NIRF provided information about NPs distribution in the whole body with high sensitivity in real-time; US and MR imaging could achieve deep-seated tumor imaging with high resolution; while PA could provide higher contrast images of the optical absorption. To sum up, PFP@tLyP-1-LIP-H(Gd) served as a NIRF/US/PA/MRI tetramodal imaging contrast agent for providing multi-hierarchy and multi-attribute information comprehensively to achieve a mistake-free diagnosis and real-time monitoring/guidance.

In vivo Programmed Therapeutic Assay

LIFU utilizes ultrasound to induce tumor cell death with both ADV and SDT mechanisms. Oxygen is essential during SDT because the ROS generation is highly oxygen-dependent, reacting with DNA breaks and preventing the damage from repairing in tumor cells. Thus, the SDT therapeutic efficacy was strictly restricted in hypoxic tumor cells. Bubbles

are essential to LIFU irradiation because they can enhance the SDT efficacy with highly hypoxia-tolerance, thus enhancing SDT-induced hypoxic tumor therapy. Hence, we evaluated in vivo tumor therapy using the MDA-MB-231 xenograft tumor model (Figure 9A). Tumor-bearing mice were intravenously injected with saline, tLyP-1-LIP, tLyP-1-LIP-H(Gd), and PFP@tLyP-1-LIP-H(Gd), and a part of them was exposed to LIFU at 0 d, 4 d and 8 d postinjection

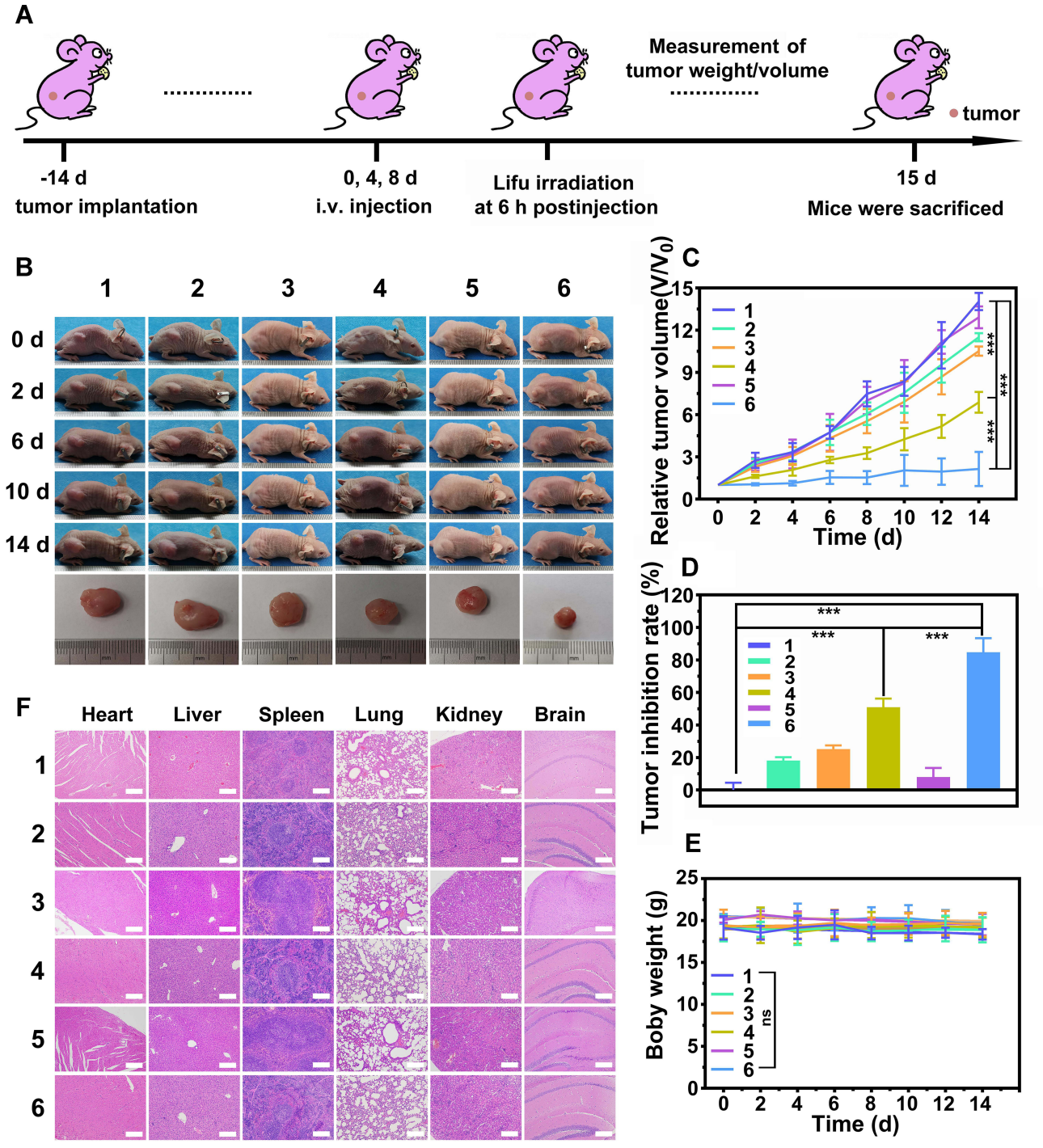

Figure 9 In vivo antitumor and therapeutic evaluation of PFP@tLyP-1-LIP-H(Gd). (**A**) Schematic illustration of the in vivo SDT process. (**B**) Pictures of representative mice in 14 days after different treatments. (**C**) Relative tumor volume changes of the mice after various treatments. (**D**) Tumor inhibition rate of the mice after multiple treatments. (**E**) Bodyweight changes of the mice after different treatments. (**F**) H&E staining results of major organs (including heart, liver, spleen, lungs, kidney, and brain) in various groups (magnitude of enlargement: 100X). (Group 1: Control, Group 2: LIFU, Group 3: tLyP-1-LIP+LIFU, Group 4: tLyP-1-LIP-H(Gd)+LIFU, Group 5: PFP@tLyP-1-LIP-H(Gd), Group 6: PFP@tLyP-1-LIP-H(Gd)+LIFU). (***$p < 0.001$ compared by one-way ANOVA analysis, n=5).

(1.6 W cm^{-2}, 3 min). The body weight and tumor size were measured every other day, and we recorded the mice's images in each group. Only moderate tumor inhibition was observed in the LIFU only group, PFP@tLyP-1-LIP-H(Gd) group, and tLyP-1-LIP+LIFU group compared to the control group (Figure 9B and C).

In contrast, the tLyP-1-LIP-H(Gd)+LIFU group showed an enhanced therapeutic effect compared to the tLyP-1-LIP +LIFU group, confirming the therapeutic effect originated from the H(Gd) induced SDT. Moreover, PFP@tLyP-1-LIP-H(Gd)+LIFU showed the maximum tumor inhibition at the end of the therapeutic process, suggesting the ideal therapeutic outcome against hypoxic tumors. The tumor inhibition rate was also calculated, further confirming the combination of ADV effect and SDT could inhibit tumor growth (Figure 9D). No apparent change in body weight was observed during the therapeutic process, indicating the therapeutic doses and LIFU intensity in our study were well-tolerated (Figure 9E). The path morphology analysis of heat, liver, spleen, lungs, and kidneys was observed, and no apparent tissue damage was found in all treatment groups (Figure 9F). Furthermore, complete blood count, liver and kidney function markers all showed negligible difference among the groups at different therapeutic times in 14 days at our tested doses (Figure S8).

To further test the programmed therapeutic effect against hypoxic tumors, tumor slices were collected from different groups of mice at 24 h after the last treatment. The slices were stained with hematoxylin and eosin (H&E) and Proliferating Cell Nuclear Antigen (PCNA) to observe the change in tumor cell morphologies, cell proliferation, and apoptosis levels. In the PFP@tLyP-1-LIP-H(Gd) + LIFU group, a large number of cell apoptosis and necrosis was observed by H&E staining. Moreover, the maximum expression of TdT-mediated dUTP Nick-End Labeling (TUNEL) and the minimal expression of PCNA were observed in the PFP@tLyP-1-LIP-H(Gd)+LIFU group (Figure 10A), further indicating the high therapeutic efficacy of PFP@tLyP-1-LIP-H(Gd). After a 4 h post intravenous injection, PFP@tLyP-1-LIP-H(Gd) can be detected away from the tumor blood vessels (labeled with CD31), while PFP@-LIP-H(Gd) without tLyP-1 mainly accumulate around the blood vessels (Figure 9B). These results indicated that the tLyP-1 could afford superior tumor penetration in tumors. To sum up, the above results were in accordance with the multimodal imaging

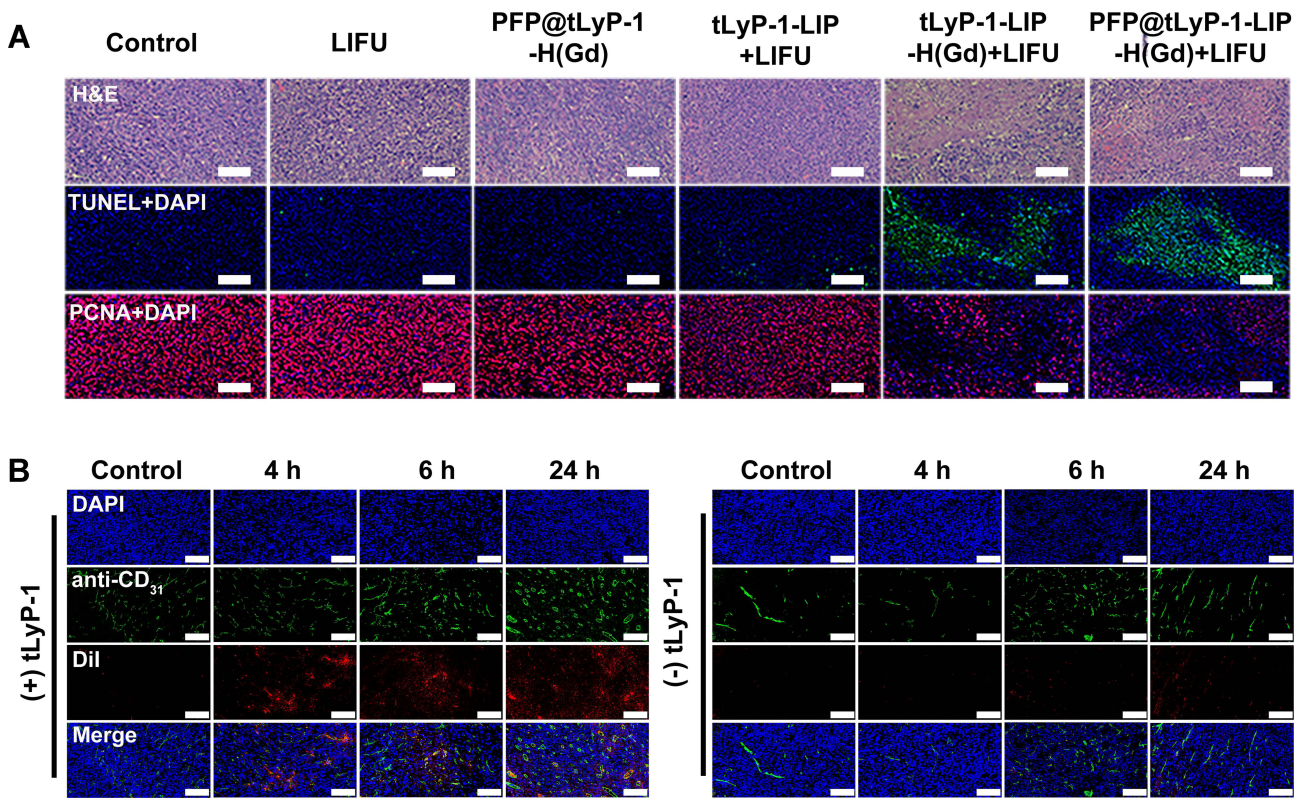

Figure 10 In vivo pathological results of tumors. (**A**) H&E, TUNEL and PCNA staining of tumor sections after different treatments. (**B**) Fluorescent staining of tumor sections at various times after intravenous injection of DiI labeled PFP@LIP-H(Gd) or PFP@tLyP-1-LIP-H(Gd).

capability and confirmed the deep-penetration effect of PFP@tLyP-1-LIP-H(Gd) as "nanobombs" for efficient tumor theranostics (Figure 10B).

Conclusions

In summary, we have successfully developed an acoustic tumor microenvironment regulating theranostic strategy based on a "liquid-to-gas" phase transition NPs to combat hypoxic tumors. The LIFU-responsive nanoplatform was constructed by incorporating PFP, acting as phase-transition materials, in the tLyP-1 functionalized liposomes, which could target deep-seated tumor cells efficiently and subsequently exert a violent "liquid-to-gas" phenomenon. tLyP-1, a short peptide for targeting nutrient deprivation tumor cells through an NRP-1-dependent endocytic/exocytic transport pathway, achieved effective deep-seated tumor infiltration. Moreover, lipid was featured with high hydrophobic agent loading efficiency and facile PFP encapsulation; thus, H(Gd) was encapsulated to perform "bomb-like" ADV effect and SDT. After low intensity focused ultrasound (LIFU) irradiation, the ADV effect of PFP@tLyP-1-LIP triggered a sharply "liquid-to-gas" phenomenon for applications in both theranostic "bomb-like" effect and ROS generation, which showed comparable therapeutic efficacy under both normoxia and hypoxia. In addition to the therapeutic applications, the prepared PFP@tLyP-1-LIP-H(Gd) could act as a US/PA/NIRF/MRI tetramodal imaging agent for guiding therapy. Therefore, this work pioneers a field to achieve hypoxia-tolerant sonodynamic therapy for synergistic deep-seated tumor therapy and offers a tetramodal imaging strategy for theranostic applications.

Supplementary Materials

Supplementary figures and tables.

Acknowledgments

The authors sincerely grateful for the financial supports from the National Natural Science Foundation of China (Grant No. 82171946, 81873901), Basic Research and Frontier Exploration Key Project of Chongqing Science and Technology Commission (Grant No. cstc2019jcyj-zdxmX0020), the project of China Postdoctoral Science Foundation (2021M690171), Guangdong Basic and Applied Basic Research Foundation (2021A1515110102), High-level Medical Reserved Personnel Training Project of Chongqing, CQMU Program for Youth Innovation in Future Medicine (W0026), Kuanren Talents Program of the Second Affiliated Hospital of Chongqing Medical University (KR2019G001), Chongqing Science and Health Joint Medical Research Project-Young and Middle-aged High-level Talent Project (2020GDRC011), and Basic Research and Frontier Exploration Project of Yuzhong District, Chongqing (20190112), Chongqing General Hospital Medical Science and Technology Innovation Project (2019ZDXM08).

Disclosure

The authors have declared that no completing interest exists.

References

1. Celli JP, Spring BQ, Rizvi I, et al. Imaging and photodynamic therapy: mechanisms, monitoring, and optimization. *Chem Rev*. 2010;110(5):2795–2838. doi:10.1021/cr900300p
2. Lucky SS, Soo KC, Zhang Y. Nanoparticles in photodynamic therapy. *Chem Rev*. 2015;115(4):1990–2042. doi:10.1021/cr5004198
3. Yang B, Chen Y, Shi J. Reactive Oxygen Species (ROS)-based nanomedicine. *Chem Rev*. 2019;119(8):4881–4985. doi:10.1021/acs.chemrev.8b00626
4. Agostinis P, Berg K, Cengel KA, et al. Photodynamic therapy of cancer: an update. *CA Cancer J Clin*. 2011;61(4):250–281. doi:10.3322/caac.20114
5. Cheng HB, Qiao B, Li H, et al. Protein-activatable diarylethene monomer as a smart trigger of noninvasive control over reversible generation of singlet oxygen: a facile, switchable, theranostic strategy for photodynamic-immunotherapy. *J Am Chem Soc*. 2021;143(5):2413–2422. doi:10.1021/jacs.0c12851
6. Yue W, Chen L, Yu L, et al. Checkpoint blockade and nanosonosensitizer-augmented noninvasive sonodynamic therapy combination reduces tumour growth and metastases in mice. *Nat Commun*. 2019;10(1):2025. doi:10.1038/s41467-019-09760-3
7. Qian X, Zheng Y, Chen Y. Micro/Nanoparticle-Augmented Sonodynamic Therapy (SDT): breaking the depth shallow of photoactivation. *Adv Mater*. 2016;28(37):8097–8129. doi:10.1002/adma.201602012
8. Wang X, Wu M, Li H, et al. Enhancing penetration ability of semiconducting polymer nanoparticles for sonodynamic therapy of large solid tumor. *Adv Sci*. 2022;9:e2104125. doi:10.1002/advs.202104125
9. Heldin CH, Rubin K, Pietras K, Ostman A. High interstitial fluid pressure - an obstacle in cancer therapy. *Nat Rev Cancer*. 2004;4(10):806–813. doi:10.1038/nrc1456

10. Lei Q, Wang SB, Hu JJ, et al. Stimuli-responsive "cluster bomb" for programmed tumor therapy. *ACS Nano*. 2017;11(7):7201–7214. doi:10.1021/acsnano.7b03088
11. Minchinton AI, Tannock IF. Drug penetration in solid tumours. *Nat Rev Cancer*. 2006;6(8):583–592. doi:10.1038/nrc1893
12. Tredan O, Galmarini CM, Patel K, Tannock IF. Drug resistance and the solid tumor microenvironment. *J Natl Cancer Inst*. 2007;99(19):1441–1454. doi:10.1093/jnci/djm135
13. Zhao C, Tong Y, Li X, et al. Photosensitive nanoparticles combining vascular-independent intratumor distribution and on-demand oxygen-depot delivery for enhanced cancer photodynamic therapy. *Small*. 2018;14(12):e1703045. doi:10.1002/smll.201703045
14. Liu JN, Bu W, Shi J. Chemical design and synthesis of functionalized probes for imaging and treating tumor hypoxia. *Chem Rev*. 2017;117(9):6160–6224. doi:10.1021/acs.chemrev.6b00525
15. Yu M, Xu X, Cai Y, Zou L, Shuai X. Perfluorohexane-cored nanodroplets for stimulations-responsive ultrasonography and O2-potentiated photodynamic therapy. *Biomaterials*. 2018;175:61–71. doi:10.1016/j.biomaterials.2018.05.019
16. Gao M, Liang C, Song X, et al. Erythrocyte-membrane-enveloped perfluorocarbon as nanoscale artificial red blood cells to relieve tumor hypoxia and enhance cancer radiotherapy. *Adv Mater*. 2017;29(35):1701429. doi:10.1002/adma.201701429
17. Xu T, Ma Y, Yuan Q, et al. Enhanced ferroptosis by oxygen-boosted phototherapy based on a 2-in-1 nanoplatform of ferrous hemoglobin for tumor synergistic therapy. *ACS Nano*. 2020;14(3):3414–3425. doi:10.1021/acsnano.9b09426
18. Kang S, Gil YG, Min DH, Jang H. Nonrecurring circuit nanozymatic enhancement of hypoxic pancreatic cancer phototherapy using speckled ru-te hollow nanorods. *ACS Nano*. 2020;14(4):4383–4394. doi:10.1021/acsnano.9b09974
19. Cao J, Qiao B, Luo Y, et al. A multimodal imaging-guided nanoreactor for cooperative combination of tumor starvation and multiple mechanism-enhanced mild temperature phototherapy. *Biomater Sci*. 2020;8(23):6561–6578. doi:10.1039/D0BM01350A
20. Phua SZF, Yang G, Lim WQ, et al. Catalase-integrated hyaluronic acid as nanocarriers for enhanced photodynamic therapy in solid tumor. *ACS Nano*. 2019;13(4):4742–4751. doi:10.1021/acsnano.9b01087
21. Xiang Q, Qiao B, Luo Y, et al. Increased photodynamic therapy sensitization in tumors using a nitric oxide-based nanoplatform with ATP-production blocking capability. *Theranostics*. 2021;11(4):1953–1969. doi:10.7150/thno.52997
22. Tang W, Yang Z, He L, et al. A hybrid semiconducting organosilica-based O2 nanoeconomizer for on-demand synergistic photothermally boosted radiotherapy. *Nat Commun*. 2021;12(1):523. doi:10.1038/s41467-020-20860-3
23. Yu W, Liu T, Zhang M, et al. O2 economizer for inhibiting cell respiration to combat the hypoxia obstacle in tumor treatments. *ACS Nano*. 2019;13(2):1784–1794. doi:10.1021/acsnano.8b07852
24. Zhang L, Wang Z, Zhang Y, et al. Erythrocyte membrane cloaked metal-organic framework nanoparticle as biomimetic nanoreactor for starvation-activated colon cancer therapy. *ACS Nano*. 2018;12(10):10201–10211. doi:10.1021/acsnano.8b05200
25. Qu J, Teng D, Sui G, et al. A photothermal-hypoxia sequentially activatable phase-change nanoagent for mitochondria-targeting tumor synergistic therapy. *Biomater Sci*. 2020;8(11):3116–3129. doi:10.1039/D0BM00003E
26. Guo Y, Jia HR, Zhang X, et al. A glucose/oxygen-exhausting nanoreactor for starvation- and hypoxia-activated sustainable and cascade chemo-chemodynamic therapy. *Small*. 2020;16(31):e2000897. doi:10.1002/smll.202000897
27. Xiang H, Lin H, Yu L, Chen Y. Hypoxia-irrelevant photonic thermodynamic cancer nanomedicine. *ACS Nano*. 2019;13(2):2223–2235. doi:10.1021/acsnano.8b08910
28. Tao N, Li H, Deng L, et al. A cascade nanozyme with amplified sonodynamic therapeutic effects through comodulation of hypoxia and immunosuppression against cancer. *ACS Nano*. 2021;16:1c07504.
29. Zhou Y, Wang Z, Chen Y, et al. Microbubbles from gas-generating perfluorohexane nanoemulsions for targeted temperature-sensitive ultrasonography and synergistic HIFU ablation of tumors. *Adv Mater*. 2013;25(30):4123–4130. doi:10.1002/adma.201301655
30. Zhong Y, Zhang Y, Xu J, et al. Low-intensity focused ultrasound-responsive phase-transitional nanoparticles for thrombolysis without vascular damage: a synergistic nonpharmaceutical strategy. *ACS Nano*. 2019;13(3):3387–3403. doi:10.1021/acsnano.8b09277
31. Tan X, Huang J, Wang Y, et al. Transformable nanosensitizer with tumor microenvironment-activated sonodynamic process and calcium release for enhanced cancer immunotherapy. *Angew Chem Int Ed Engl*. 2021;60(25):14051–14059. doi:10.1002/anie.202102703
32. He H, Du L, Guo H, et al. Redox responsive metal organic framework nanoparticles induces ferroptosis for cancer therapy. *Small*. 2020;16(33):e2001251. doi:10.1002/smll.202001251
33. Zhao H, Wu M, Zhu L, et al. Cell-penetrating peptide-modified targeted drug-loaded phase-transformation lipid nanoparticles combined with low-intensity focused ultrasound for precision theranostics against hepatocellular carcinoma. *Theranostics*. 2018;8(7):1892–1910. doi:10.7150/thno.22386
34. Zhang N, Cai X, Gao W, et al. A multifunctional theranostic nanoagent for dual-mode image-guided HIFU/chemo- synergistic cancer therapy. *Theranostics*. 2016;6(3):404–417. doi:10.7150/thno.13478
35. Liu T, Zhang N, Wang Z, et al. Endogenous catalytic generation of O2 bubbles for in situ ultrasound-guided high intensity focused ultrasound ablation. *ACS Nano*. 2017;11(9):9093–9102. doi:10.1021/acsnano.7b03772
36. Lu X, Zhao J, Wang Q, et al. Sonolytic degradation of bisphenol S: effect of dissolved oxygen and peroxydisulfate, oxidation products and acute toxicity. *Water Res*. 2019;165:114969. doi:10.1016/j.watres.2019.114969
37. Torabi Angaji M, Ghiaee R. Decontamination of unsymmetrical dimethylhydrazine waste water by hydrodynamic cavitation-induced advanced Fenton process. *Ultrason Sonochem*. 2015;23:257–265. doi:10.1016/j.ultsonch.2014.09.007
38. Tao Y, Cai J, Huai X, Liu B. A novel antibiotic wastewater degradation technique combining cavitating jets impingement with multiple synergetic methods. *Ultrason Sonochem*. 2018;44:36–44. doi:10.1016/j.ultsonch.2018.02.008
39. Pang HB, Braun GB, Friman T, et al. An endocytosis pathway initiated through neuropilin-1 and regulated by nutrient availability. *Nat Commun*. 2014;5:4904. doi:10.1038/ncomms5904
40. Chen J, Ding J, Wang Y, et al. Sequentially responsive shell-stacked nanoparticles for deep penetration into solid tumors. *Adv Mater*. 2017;29(32):1701170. doi:10.1002/adma.201701170
41. Huo D, Jiang X, Hu Y. Recent advances in nanostrategies capable of overcoming biological barriers for tumor management. *Adv Mater*. 2020;32(27):e1904337. doi:10.1002/adma.201904337
42. Fan W, Huang P, Chen X. Overcoming the Achilles' heel of photodynamic therapy. *Chem Soc Rev*. 2016;45(23):6488–6519. doi:10.1039/C6CS00616G
43. Moore C, Chen F, Wang J, Jokerst JV. Listening for the therapeutic window: advances in drug delivery utilizing photoacoustic imaging. *Adv Drug Deliv Rev*. 2019;144:78–89. doi:10.1016/j.addr.2019.07.003

44. Luo Y, Qiao B, Zhang P, et al. TME-activatable theranostic nanoplatform with ATP burning capability for tumor sensitization and synergistic therapy. *Theranostics*. 2020;10(15):6987–7001. doi:10.7150/thno.44569
45. Qiao B, Luo Y, Cheng HB, et al. Artificial nanotargeted cells with stable photothermal performance for multimodal imaging-guided tumor-specific therapy. *ACS Nano*. 2020;14(10):12652–12667. doi:10.1021/acsnano.0c00771
46. Shin TH, Choi Y, Kim S, Cheon J. Recent advances in magnetic nanoparticle-based multi-modal imaging. *Chem Soc Rev*. 2015;44(14):4501–4516. doi:10.1039/C4CS00345D
47. Li X, Kim J, Yoon J, Chen X. Cancer-associated, stimuli-driven, turn on theranostics for multimodality imaging and therapy. *Adv Mater*. 2017;29 (23):1606857.
48. Lovell JF, Jin CS, Huynh E, et al. Porphysome nanovesicles generated by porphyrin bilayers for use as multimodal biophotonic contrast agents. *Nat Mater*. 2011;10(4):324–332. doi:10.1038/nmat2986